



Enhancing energy conversion performances in standing-wave thermoacoustic engine with externally forcing periodic oscillations

Lixian Guo^a, Dan Zhao^{a,*}, Li Cheng^b, Xu Dong^c, Jingyuan Xu^d

^a Department of Mechanical Engineering, Faculty of Engineering, University of Canterbury, Private Bag 4800, Christchurch, 8041, New Zealand

^b Department of Mechanical Engineering, The Hong Kong Polytechnic University, Hung Hom, Kowloon, Hong Kong SAR, China

^c Research Institute of Aero-engine, Beihang University, No. 37 Xueyuan Road, Beijing, 100191, China

^d Mechanical and Electrical Engineering Division, Karlsruhe Institute of Technology, Karlsruhe, 76344, Germany

ARTICLE INFO

Handling Editor: Ruzhu Wang

Keywords:

Thermoacoustics
Thermoacoustic engine
Thermodynamics
Heat transfer
Nonlinear dynamics

ABSTRACT

The present work focuses on enhancing thermo-acoustics energy conversion performance and nonlinear dynamics of heat-driven acoustics oscillations in standing-wave thermoacoustic engines (SWTAE) in the presence of externally forcing perturbations. Such perturbations could be applied in either pressure or velocity fluctuations. 2D numerical SWTAE models are developed and validated, and then applied to examine the effects of 1) the forcing perturbation frequencies, 2) its amplitudes, and 3) the inlet diameter of applying such perturbations on heat-driven acoustics behavior. Our results show that pressure perturbations attenuate heat-driven acoustic limit cycles, while forcing velocity perturbations at a specific frequency range can enhance the thermo-acoustics conversion in the SWTAEs. Our results also show that frequency lock-in is observed, when the ratio of the forcing velocity perturbations' energy to the self-excited acoustical energy is ranged from 0.11 to 0.66. Furthermore, Hopf supercritical bifurcations are observed, resulting in transitions from steady state to quasi-periodic and limit cycle oscillations. As the forcing perturbation frequency is approaching to that of the self-excited heat-driven acoustic oscillations (i.e. the ratio of the forcing frequency to that of self-excited oscillations is ranged from 0.89 to 1.11), apparent improvements are observed on the output heat-driven acoustic power and thermo-acoustic energy conversion efficiency, especially when the two frequencies are coincided (i.e. ~180 Hz). Increasing the forcing perturbation's energy or enlarging the inlet diameter of applying such perturbations further enhances these improvements. Overall, the developed numerical model may serve as a valuable tool for predicting the heat-driven acoustic power output from a SWTAE in the presence of externally forcing perturbations.

1. Introduction

Considerable efforts to reduce dependence on fossil fuels have led to increased interest in thermoacoustic engines (TAE) for their potential to contribute to energy conservation using low-grade and renewable energy sources [1–3]. The basic physical principle of the TAE is the 'thermoacoustic effect', which was first qualitatively explained by Lord Rayleigh [4]. According to the phase difference between acoustic pressure and velocity oscillations, the TAE is classified into 2 types. One is the standing-wave thermoacoustic engine (SWTAE) and the other is traveling-wave thermoacoustic engine (TWTAE) [5,6]. Due to its simplicity and compact design, the SWTAE has been extensively studied in previous researches [7–9], so it is more likely to be used in energy

industry and the present study considers SWTAE. To broaden the application scope of SWTAE, previous researches primarily concentrated on improving its acoustic oscillation characteristics and thermal efficiency [10–12]. For this, operational conditions, such as the type of working gases [13,14], the mean pressure [15,16], and the temperature differences across the stack [16,17], are explored as research subjects to optimize SWTAE performance. Previous research results indicate that the acoustic oscillations characteristics of the SWTAE are higher with an increase in the molecular weight of the working gas, the mean pressure, and the temperature difference across the stack [18,19]. Additionally, previous studies also investigated the influence of geometric parameters on the performance of the SWTAE [20], revealing that the performance of the thermo-acoustics system with the cone-shaped resonance tube is better than those with the cylindrical one [21–23].

* Corresponding author.

E-mail address: dan.zhao@canterbury.ac.nz (D. Zhao).

<https://doi.org/10.1016/j.energy.2024.130634>

Received 22 November 2023; Received in revised form 31 December 2023; Accepted 6 February 2024

Available online 7 February 2024

0360-5442/© 2024 The Authors. Published by Elsevier Ltd. This is an open access article under the CC BY license (<http://creativecommons.org/licenses/by/4.0/>).

Nomenclature	
A	Cross-sectional area [m ²]
C_p	Isobaric specific heat [J/kg·K]
d_i	Forced flow inlet diameter [mm]
$D0, \dots, D4$	TAE models with varying forced inlet diameters
D	Engine diameter [mm]
E_{af}	Externally forcing energy of the periodic pressure/velocity [J]
\dot{E}_{af}	Externally forcing power of the periodic pressure/velocity [W]
E_{as}	Self-excited oscillation energy of the TAE [J]
$F(t)$	Oscillation growth rate function
f_{Rn}	n th-order acoustic oscillation frequency [Hz]
f_{Rd}	Dominant oscillation frequency [Hz]
f_s	Self-excited frequency of the TAE [Hz]
f_f	Forced frequency [Hz]
f_{fc}	Critical forced frequency in bifurcation [Hz]
$I(\omega)$	Acoustic power [W]
$\hat{I}_{1A}(\omega)$	Fundamental-mode acoustic power amplitude [W]
L	Length of the engine [m]
L_H	Hot buffer length [m]
L_S	Stack length [m]
L_{sm}	The middle position of the stack [m]
L_{sl}	Left end of the stack [m]
L_{sr}	Right end of the stack [m]
L_R	Resonator length [m]
p	Pressure [Pa]
p_f	Forced periodic pressure
p_{fA}	Forced pressure amplitude [Pa]
p'	Acoustic oscillation pressure [Pa]
p_i	Initial pressure [Pa]
$ p'_{rms}(\omega) $	The root mean square value of the fluctuation oscillation pressure [Pa]
p_{ref}	Standard reference sound pressure [Pa]
p'_A	The limit cycle oscillations' pressure amplitude [Pa]
\hat{p}_{nA}	n th-order pressure amplitudes of the decomposed oscillation pressure [Pa]
\hat{p}_{nAT}	n th-order theoretical pressure amplitudes of the decomposed oscillation pressure [Pa]
\dot{q}_t	Transversal heat flux [W/m ²]
\dot{Q}_{in}	Input heat power [W]
R	Gas constant [J/K • kg]
$SPL(\omega)$	Sound pressure level [dB]
T	Gas temperature [K]
T_h	Hot end temperature of the stack [K]
T_c	Cold end temperature of the stack [K]
T_s	Wall temperature of the stack [K]
t	Time [s]
t_s	Stack thickness [mm]
t_p	Plate spacing [mm]
v	Velocity [m/s]
v_f	Forced periodic velocity
v'_A	The limit cycle oscillations' velocity amplitude [m/s]
v_{fA}	Forced velocity amplitude [m/s]
v_{hy}	Tested case of forced velocity
<i>Greek symbols</i>	
α	Any instantaneous thermodynamic variable
$\bar{\alpha}$	Time-averaged component of any instantaneous thermodynamic variable
α'	Fluctuating component of any instantaneous thermodynamic variable
$\hat{\alpha}_n$	n th-order components of any instantaneous thermodynamic variable after Fast Fourier Transform algorithm analysis
β	Thermal expansion coefficient [1/K]
γ	Adiabatic index of the gas
$\Delta p'$	Pressure gradient [Pa]
γ_E	The ratio between the acoustic energy of the forced periodic velocity and that of the self-excited oscillation of the TAE
ω_{Rd}	Angular frequency [rad/s]
δ_k	Thermal penetration depth [mm]
δ_g	Oscillation growth rate
η_f	Thermal efficiency
κ	Thermal conductivity [W/m·K]
Γ	The ratio of the actual temperature gradient to the onset critical temperature gradient
ρ	Density of fluid [kg/m ³]
φ	Phase over a complete acoustic period/cycle
$ \Delta x$	Plate surface area
<i>Abbreviation</i>	
CFD	Computational Fluid Dynamics
FFT	Fast Fourier Transform
LES	Large Eddy Simulation
TAE	Thermoacoustic Engine
SWTAE	Standing-wave Thermoacoustic Engine
TWTAE	Traveling-wave Thermoacoustic Engine
UDF	User Defined Function
URANS	Unsteady Reynolds Averaged Navier Stokes

The investigation methodologies of SWTAE and TWTAE include not only conventional theoretical and experimental research methods, but also Computational Fluid Dynamics (CFD) simulations. CFD is recognized as a valuable numerical tool for simulating TAEs through the comparison of its results with experimental data [24,25] in details. It has the attractive feature and capability of exploring nonlinear phenomena of heat-driven flow fields [26,27]. The nonlinear behaviors as observed from SWTAE, including vortex formation, bistability, and mode transitions, and their impact on SWTAE performances are revealed through detailed CFD investigations [28–30]. However, further insightful exploration is still needed in certain aspects of the SWTAE. Previous researches indicate that externally forcing energy exhibits a significant impact on the pressure-gradient-driven flow, mitigating the effects of thermoacoustic instabilities in the combustion system [31,32]. Thus, external perturbations can be introduced to control self-excited

thermoacoustic phenomena and so affect thermal-acoustic energy conversion efficiency [33–35]. However, to the best knowledge of the present authors, few studies have been reported in the literature on developing an effective model that can reasonably simulate TAEs with forcing perturbations.

There are current interests in thermo-acoustic communities in knowing whether these externally applied forcing perturbations can enhance thermo-acoustic energy conversion performances in SWTAE systems. Therefore, the current study aims to establish a TAE numerical model that can accurately investigate the impact of externally forcing perturbations on the self-excited heat-driven acoustic oscillations characteristics and shed lights on the detailed flow characteristics of the TAE. For this, we first create a full-scale SWTAE model, and then conduct both URANS (Unsteady Reynolds Averaged Navier-Stokes) and LES (Large Eddy Simulation) investigations on the modelled SWTAE. With the

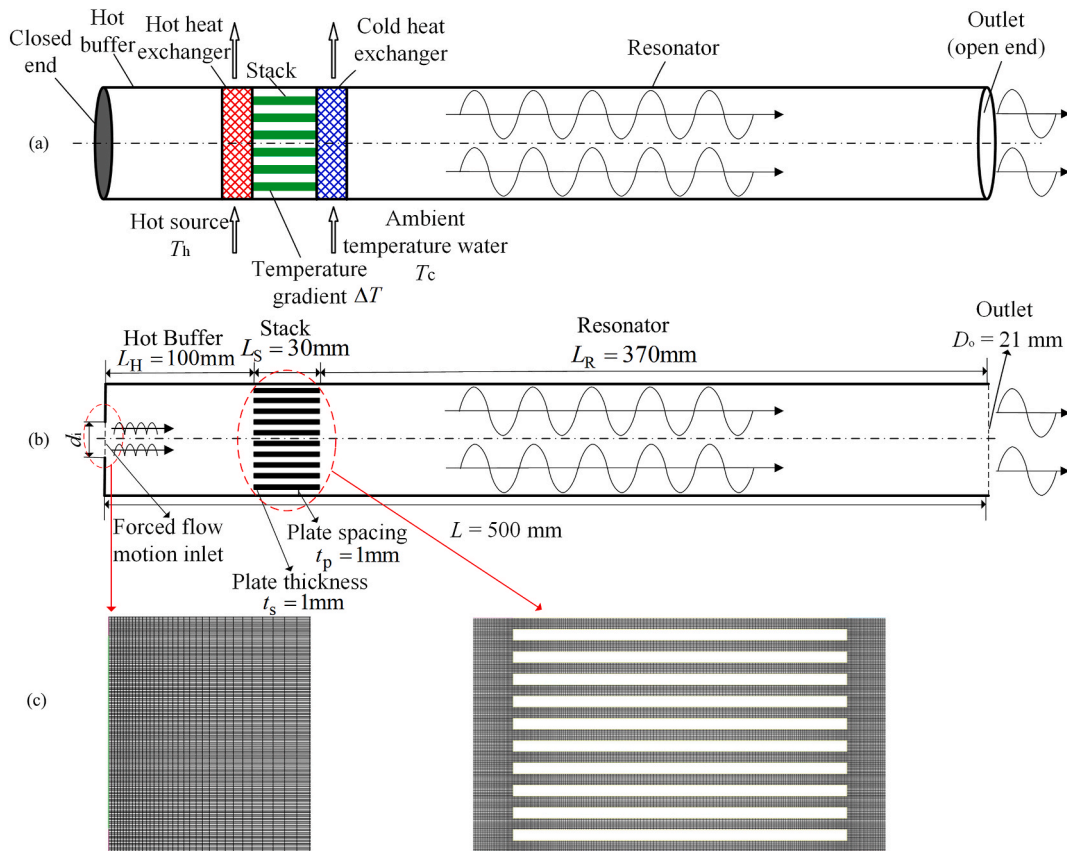


Fig. 1. (a) Schematic drawing of the 3D standing-wave thermoacoustic engine (SWTAE) model, (b) 2D computational domain of the full-scale SWTAE model, (c) the mesh configurations in/around the inlet and stack regions.

Table 1
Geometric dimensions and thermophysical properties of the established TAE model.

Engine/gas parameters	Value/law
Diameter D	21 mm
Hot buffer length L_H	0.1 m
Stack length L_S	0.03 m
Resonator length L_R	0.37 m
Stack plate thickness t_s	1 mm
Stack plate spacing t_p	1 mm
Idea-gas constant R	287 J/kg·K
Specific heat	Piecewise-polynomial
Molecular weight	28.966 kg/k·mol
Thermal conductivity κ	0.0242 W/m·K

model validated, we then examine the effects of (1) the inlet diameter of externally applying thermodynamic perturbations, (2) the externally applied pressure or velocity perturbations, and (3) the amplitude and frequency of the externally forcing flow perturbations on the SWTAE performances. The present work is concerned with comparison studies on the acoustic output performance and thermodynamics of the SWTAE with externally forcing perturbations, and exploring the nonlinear phenomena and limit cycles observed from the modelled thermoacoustic system.

The rest of this paper is organized as follows: Section 2 describes the development of full-scale SWTAE models and validation. Externally forcing flow motions are applied to the modelled SWTAE with varying inlet diameters in Section 3. In Section 4, externally forced periodic oscillations with different frequencies and amplitudes are implemented on the modelled SWTAE, and the corresponding nonlinear phenomena are observed. Finally, concluding remarks and potential further studies

are summarized in Section 5.

2. Numerical methodology

2.1. Description of the numerical model

The schematic diagram of the quarter-wavelength SWTAE is shown in Fig. 1(a). The TAE comprises a hot buffer, two heat exchangers placed on either side of the stack, and an acoustic resonator [36,37]. The stack consists of ten parallel solid plates, with equal stack thickness t_s and plate spacing t_p in the axial direction. The right end of the engine is open to the environment, serving as the outlet. As suggested by Zink's research [38], the heat exchangers on both sides of the stack in the simulation can be omitted. The linear temperature gradient is imposed on the stack by prescribing User Defined Functions (UDF), with the left end of the stack at 700 K (T_h) and the right end at 300 K (T_c). The hot buffer wall is set to 700 K, while all other surfaces are modelled as the adiabatic walls. To investigate the impact of forcing perturbations on the performance of the TAE, the pressure or velocity inlet with a varying diameter d_i ranging from 0 to D (the diameter of the engine), is set at the left end of the engine, while the rest of the left end is rigidly closed. High-quality structured meshes with uniform cell sizes and smooth transitions between different mesh regions are employed in the computational domain with the use of ICEM (a mesh generation tool offered by ANSYS). A finer mesh is applied in/around the inlet and stack regions of the TAE, as shown in Fig. 1(c). The minimum mesh size in the near-wall region is guaranteed to be smaller than the viscous and thermal penetration depths to accurately capture thermoacoustic effects [39,40]. The SWTAE utilizes air as the working fluid with the working pressure of $p = 101,325$ Pa. The working fluid is defined as the ideal gas, which can be expressed as $p = \rho RT$, where p , ρ , R and T denote pressure,

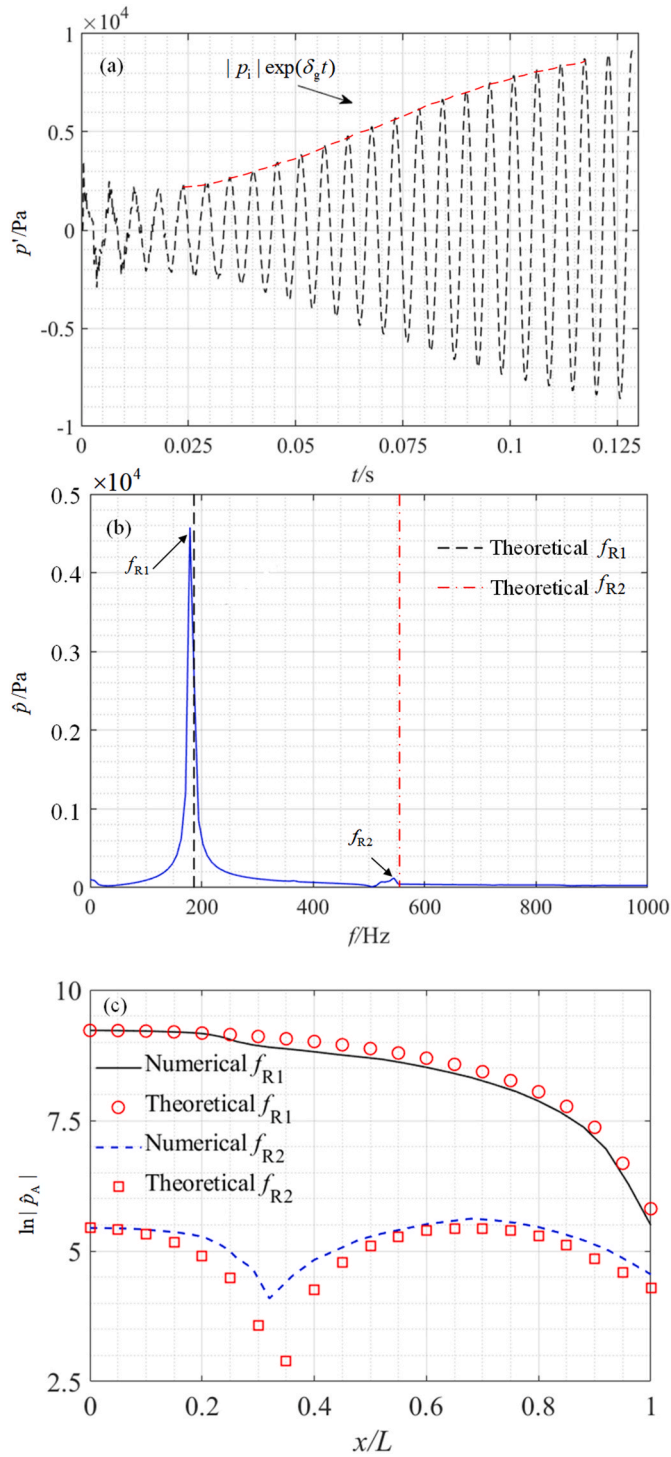


Fig. 2. The $k-\epsilon$ simulation results of (a) time evolution of the acoustic pressure fluctuations of the TAE in the initial exponential growth stage, with the growth rate function $F(t)$, (b) frequency spectrum of the acoustic pressure fluctuations and corresponding theoretical frequencies in the initial stage and (c) comparison of the longitudinal mode-shapes of the fundamental and 1st harmonic mode of acoustic pressure, illustrating both numerical and theoretical results during the ‘saturated’ limit cycle oscillations.

density, gas constant and temperature, respectively. The geometric dimensions of SWTAE and the working medium parameters are summarized in Table 1. The numerical solutions are determined using the Pressure-Velocity Coupling algorithm, selected for its low computational cost in segregated algorithms. PISO and PRESTO schemes are

Table 2

A summary of the externally forcing pressure perturbations’ amplitude (p_{iA}), velocity perturbation’s amplitude (v_{iA}) and frequency (f_i), which are imposed on the SWTAE model.

	$v_{iA}/\text{m/s}$	p_{iA}/Pa	f_i/Hz
p_{f1}/Pa	0	50	0.1
p_{f2}/Pa	0	50	180
$v_{f1}/\text{m/s}$	2.5	0	0.1
$v_{f2}/\text{m/s}$	2.5	0	180

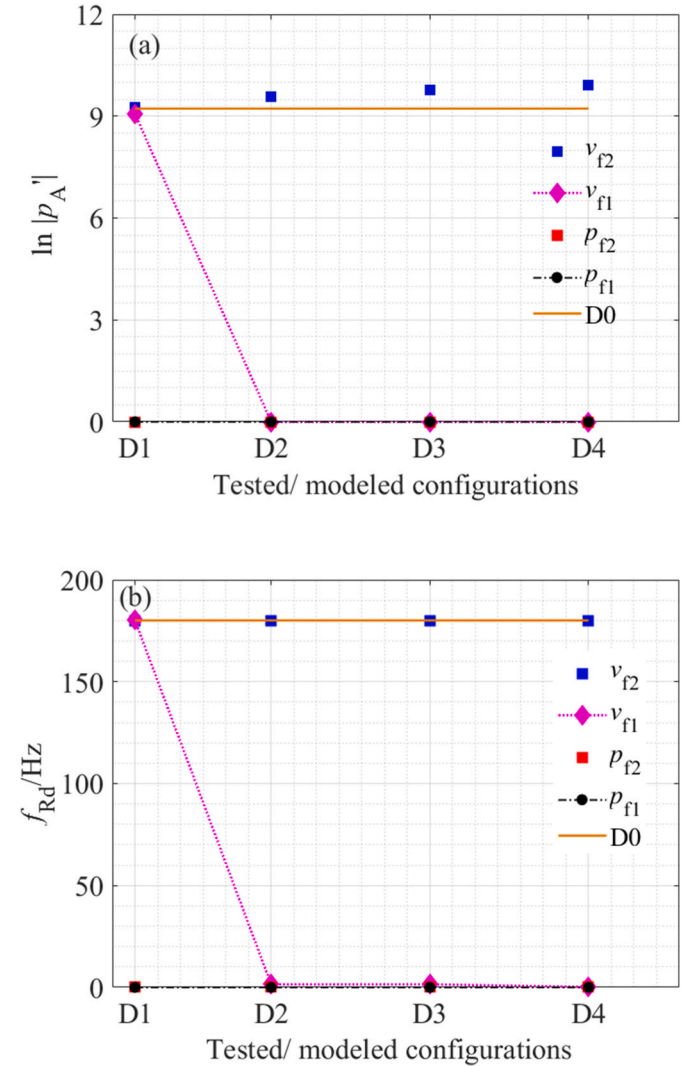


Fig. 3. Effect of the inlet diameter on the limit cycle oscillations (a) acoustic pressure amplitude and (b) the corresponding dominant frequency for TAE models D1–D4, induced by forcing pressure/velocity perturbations’ at the inlet p_{f1} , p_{f2} , v_{f1} and v_{f2} , with D0 representing the reference case of the unforced modelled SWTAE.

employed for the pressure discretization and pressure-velocity formulation, respectively. To ensure the simulation accuracy, the Second Order Upwind Scheme is chosen for all flow variables. To ensure the convergence of the simulation results, the relaxation factors for the pressure, density, body forces, momentum, turbulent kinetic energy, turbulent dissipation rate, turbulent viscosity and energy are set to 0.3, 1, 1, 0.7, 0.8, 0.8, 1, and 1, respectively. The number of nodes and the time step are set to 1.4×10^5 and 1.0×10^{-5} s, respectively. The relevant governing equations and the mesh- and time-independence studies are included in the Supplementary Material.

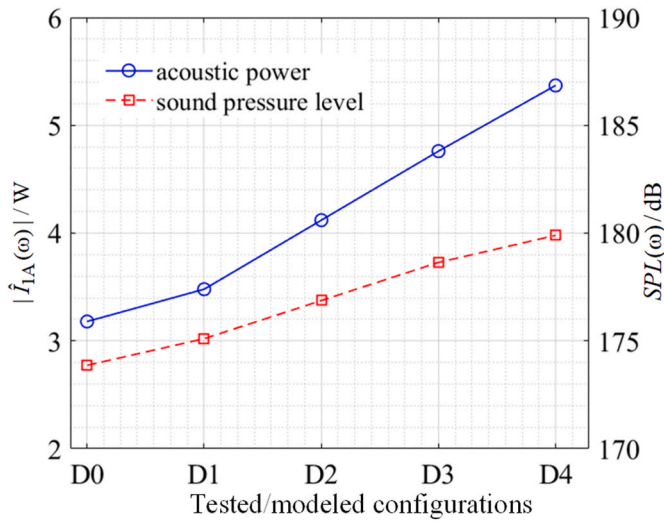


Fig. 4. Effect of the inlet diameter on the absolute value of the fundamental-mode acoustic power amplitude and sound pressure level of TAE models D0-D4, induced by forcing velocity perturbations v_{t2} .

2.2. Model validation

The simulation results of the present SWTAE predicted by different turbulence models are compared and summarized in the Supplementary Material. Through the comparison studies, the standard $k-\epsilon$ model of URANS is adopted, which has been widely applied in SWTAE simulations and yielded favorable results in comparison with the experimental data [41,42]. In Reynolds-averaging methods, all instantaneous thermodynamic variables (α) can be expressed as,

$$\alpha = \bar{\alpha} + \alpha' \quad (1)$$

where $\bar{\alpha}$ and α' represent the mean (time-averaged) and fluctuating parts. The acoustic oscillation pressure (p') undergoes an exponential increase after a short period of energy accumulation [43,44], as shown in Fig. 2(a). The reduced-order network theoretical model is established for comparison evaluations [45]. The results of the reduced-order network model align with the previous experimental measurements [46] in terms of the frequency $\omega_{Rd}/2\pi$ and the growth rate δ_g . The exponential growing process is described by the oscillations' growth rate function $F(t) = |p_i|e^{\delta_g t}$, where $|p_i|$ is the initial pressure. It is set to 10 Pa in this present work [47]. The fluctuating oscillation characteristics (α') are subject to Fast Fourier Transform (FFT) algorithm analysis to decompose it into the fundamental mode ($\hat{\alpha}_1$) and n th-order harmonic components ($\hat{\alpha}_n$) in the frequency domain. Each mode component corresponds to a resonance frequency (f_{R1}, \dots, f_{Rn}), and the frequency of the dominant mode is referred to as f_{Rd} . The fundamental and second-order frequencies of the oscillation during the growth stage (f_{R1} and f_{R2}) and the corresponding theoretical results are presented in Fig. 2(b). After the initial exponential increase stage, the limit cycle oscillation is finally generated in the TAE system [48]. Fig. 2(c) displays the longitudinal mode-shapes of the fundamental and the 1st harmonic mode of the decomposed pressure oscillations ($|\hat{p}_{1A}|$ and $|\hat{p}_{2A}|$). Moreover, according to Swift's theory [45], the theoretical fundamental and the 1st harmonic pressure ($|\hat{p}_{1AT}|$ and $|\hat{p}_{2AT}|$) mode-shapes in a one-quarter wavelength TAE are also displayed. It can be expressed as follows:

$$|\hat{p}_{1AT}| = |\hat{p}_{1A}|_{\text{peak}} \sin\left(\frac{\omega_{Rd}(L-x)}{4f_{Rd}L}\right) \quad (2a)$$

$$|\hat{p}_{2AT}| = |\hat{p}_{2A}|_{\text{peak}} \sin\left(\frac{3\omega_{Rd}(L-x)}{4f_{Rd}L}\right) \quad (2b)$$

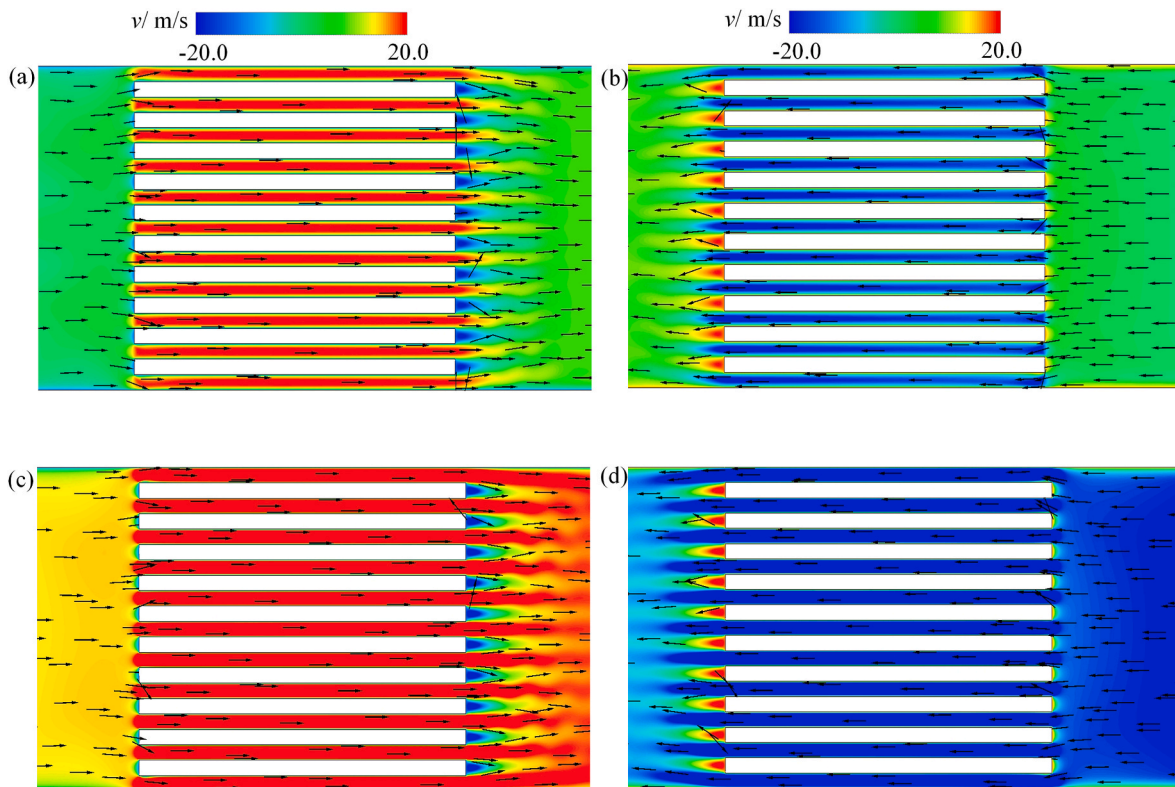


Fig. 5. Effect of the inlet diameter on the flow velocity contours around the stack area, obtained from different inlet TAE models at velocity anti-node phases, (a) D1 at φ_2 , (b) D1 at φ_4 , (c) D4 at φ_2 and (d) D4 at φ_4 , respectively.

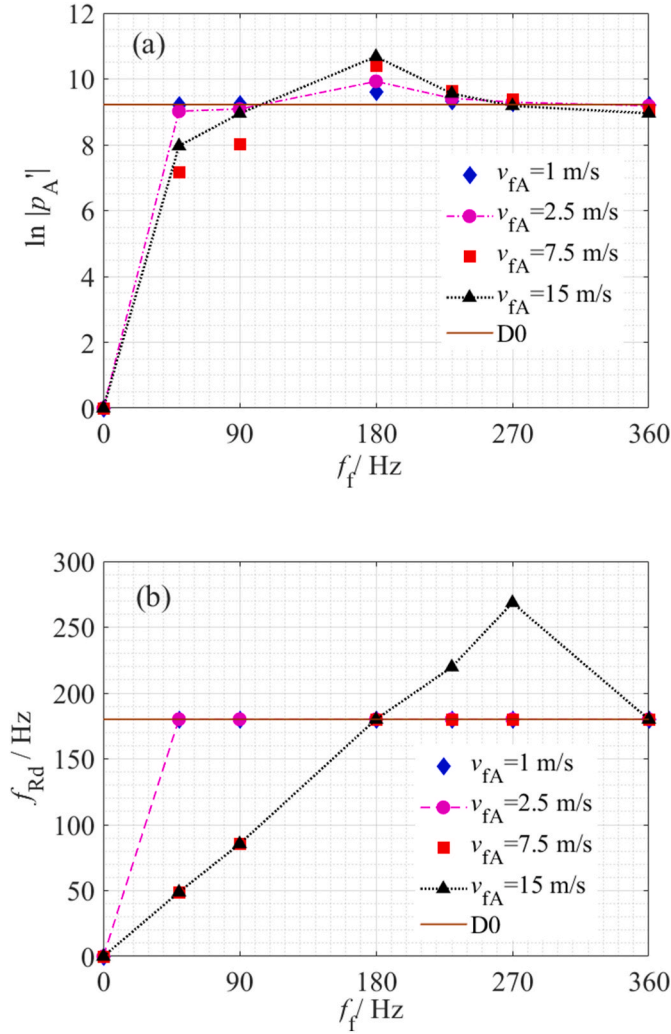


Fig. 6. Effect of different forcing perturbations amplitudes (1 m/s, 2.5 m/s, 7.5 m/s, and 15 m/s) and frequencies (0.1 Hz, 50 Hz, 90 Hz, 180 Hz, 230 Hz, 270 Hz, and 360 Hz) of forcing periodic velocity perturbations on the limit cycle oscillations (a) acoustic pressure amplitude and (b) corresponding the dominant frequency of the TAE model, with D0 lines representing the reference case of the unforced SWTAE model.

where ω_{Rd} is the dominant angular resonance frequency, expressed as $\omega_{Rd} = 2\pi f_{Rd}'$. It can be seen from Fig. 2(c) that the longitudinal mode-shapes of the acoustic pressure obtained from the SWTAE model predicted by k - ε match well with the theoretical model.

3. Effect of the inlet diameter of forcing energy on TAE output performances

The following section investigates the effects of altering the inlet diameter (d_i) of forced oscillations on TAE's overall performance. Specifically, four TAE models are examined, where d_i is set to 1 mm, 7 mm, 14 mm, and 21 mm, and are labeled as D1, D2, D3, and D4, respectively. Meanwhile, the TAE model without any inlet (i.e., $d_i = 0$) is labeled as D0.

3.1. Acoustic characteristics of the TAE with different inlet diameters

The externally forcing perturbations with a total energy (E_{af}) are imposed at the inlet of the four SWTAE models (D1-D4). The perturbations could be applied either in terms of pressure (p_r) and velocity perturbations (v_r). They can be expressed as:

$$p_r = p_{rA} \cdot \sin(2\pi \cdot f_r \cdot t) \quad (3a)$$

$$v_r = v_{rA} \cdot \sin(2\pi \cdot f_r \cdot t) \quad (3b)$$

$$E_{af} = \frac{p_{rA}^2}{2 \cdot \gamma \cdot \bar{p}} \quad (3c)$$

$$E_{af} = \rho \cdot v_{rA}^2 \cdot A \quad (3d)$$

where p_{rA} , v_{rA} and f_r are externally forcing pressure perturbation's amplitude, velocity perturbation's amplitude and frequency, respectively. A , γ , \bar{p} and t are cross-sectional area, adiabatic index of the gas, mean pressure (101,325 Pa) and time, respectively. v_{fA} , p_{fA} and f_f' of the externally forcing oscillations applied on the SWTAE models D1, D2, D3 and D4 are summarized in Table 2. The absolute values of natural logarithm-based limit cycle oscillation pressure amplitude ($\ln |p_A'|$) and corresponding dominant frequency (f_{Rd}') of forced TAE models under p_{f1} , p_{f2} , v_{f1} and v_{f2} are shown in Fig. 3. $\ln |p_A'|$ and f_{Rd}' of the unforced SWTAE (D0) system are chosen as the reference. It can be seen that $|p_A'|$ of D1-D4 with externally forcing pressure p_{f1} and p_{f2} is 0. This phenomenon is referred to as 'damping' in the SWTAE system. Damping is also occurred in TAE models D2, D3 and D4 under v_{f1} . This indicates that forced velocity or pressure, regardless of the inlet diameter, can cause the attenuation of the thermoacoustic oscillation effect by breaking up the coupling between thermal and acoustics, resulting in damping in the forced TAE system [49,50]. On the other hand, $|p_A'|$ is increased linearly with the increase of the inlet diameter under v_{f2} . Specifically, $|p_A'|$ of D4 is 101.91% and 94.28% higher than that of D0 and D1 under v_{f2} , respectively. This suggests that forced periodic velocity inlets can enhance the thermoacoustic oscillation effect in the TAE. Moreover, the larger the inlet diameter of the forced velocity flow, the more pronounced the influence on $|p_A'|$. It can also be observed from Fig. 3(b) that f_{Rd}' of the TAE under v_{f2} remains unchanged compared to D0, regardless of the variation in the inlet diameter.

The acoustic power represents the ability of the SWTAE to convert heat sources into acoustic energy. Since the thermoacoustic effect is concentrated in the stack area, the amplitude of the acoustic power of the TAE system is obtained at the right end of the stack [51]. The absolute value of the fundamental-mode acoustic power amplitude ($|\hat{I}_{1A}(\omega)|$) can be calculated as

$$|\hat{I}_{1A}(\omega)| = \frac{1}{4} \delta_k \prod \Delta x \frac{2\pi f_{Rd}' T \beta^2}{C_p} \left| \hat{p}_{1A} \right| (\Gamma - 1) \quad (4)$$

where δ_k , $\prod \Delta x$, C_p and β are thermal penetration depth, stack plate surface area, isobaric specific heat and thermal expansion coefficient, respectively. $|\hat{p}_{1A}|$ is the absolute value of the fundamental-mode pressure amplitude. Γ is the ratio of the temperature gradient of the stack (ΔT) to the onset critical temperature gradient (ΔT_{crit}) of the TAE, which is approximately 2.16 in this study. $|\hat{I}_{1A}(\omega)|$ is proportional to the volume $\prod \delta_k \Delta x$ of fluid, which is approximately within a thermal penetration depth δ_k from the plate. Additionally, the sound pressure level ($SPL(\omega)$) is introduced to display the magnitude of each component, which is expressed as

$$SPL(\omega) = 20 \log_{10} \frac{||p'_{rms}(\omega)||}{p_{ref}} \quad (5)$$

where p_{ref} is the standard reference sound pressure, typically taken as 20 μPa ($p_{ref} = 2.0 \times 10^{-5} \text{ Pa}$). $||p'_{rms}(\omega)||$ is the root mean square value of the fluctuation component of the oscillation pressure. To further investigate the acoustic output characteristics of the modelled SWTAE with different inlet diameters, Fig. 4 presents $|\hat{I}_{1A}(\omega)|$ and $SPL(\omega)$ in various inlet TAE models (D1-D4) with externally forcing velocity perturbations v_{f2} . It can be seen from Fig. 4 that $|\hat{I}_{1A}(\omega)|$ and $SPL(\omega)$ are increased

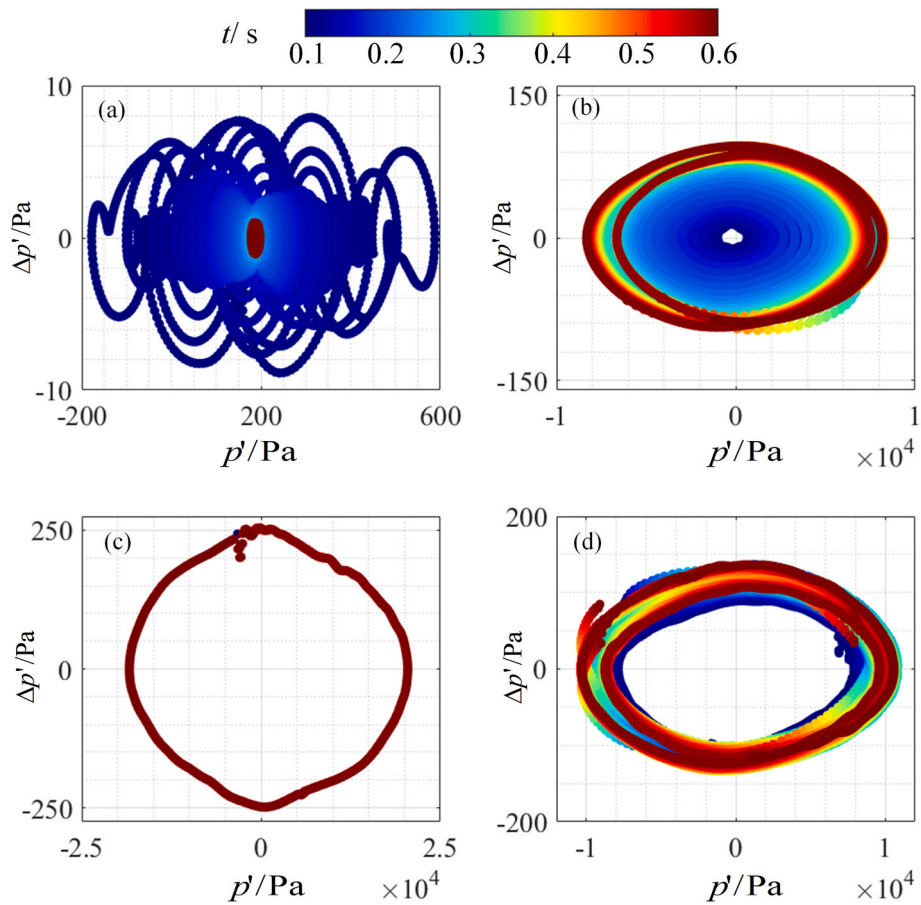


Fig. 7. Effect of forced velocity on phase diagrams illustrating the acoustic pressure fluctuations of the TAE over a span from 0.1 s to 0.6 s, with the forced velocity amplitude of 2.5 m/s at (a) 0.1 Hz (b) 90 Hz (c) 180 Hz and (d) 270 Hz.

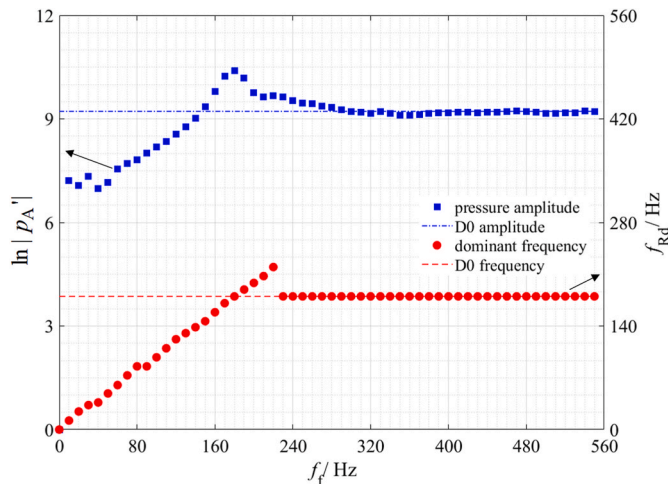


Fig. 8. Effect of forced periodic velocity on the acoustic oscillations pressure amplitude and dominant frequency of the TAE, induced by the forced velocity amplitude of 7.5 m/s and frequency ranging from 0 to 550 Hz at intervals of 10 Hz, with D0 lines representing relevant values of the unforced TAE model.

linearly with increased d_i . Specifically, $|\widehat{I}_{1A}(\omega)|$ of D4 is increased by 68.87% and 54.31% compared to that of D0 and D1, respectively. $SPL(\omega)$ of D4 (179.90 dB) is the largest, followed by D3 (178.59 dB), while that of D0 (173.87 dB) is the smallest.

3.2. Instantaneous velocity characteristics of the TAE with different inlet diameters

The stack is the crucial component for thermal-acoustic energy conversion in such TAE systems [52–54]. The implementation of the stack causes multi-dimensional flow effects due to the abrupt decrease in flow area, which subsequently impacts the thermo-acoustic conversion process of the TAE [55]. Therefore, the flow fields around the stack area in the TAE under v_{t2} are presented. Phases φ_1 to φ_4 with an interval of a quarter period over a complete acoustic cycle are chosen to display the flow fields. Phases φ_1 and φ_3 correspond to velocity nodes, and φ_2 and φ_4 indicate velocity anti-nodes. For comparison, the studied models D1 and D4 at the moments when the velocity reaches its maximum, (i.e., φ_2 and φ_4) are selected, as shown in Fig. 5. The direction of the velocity vectors in Fig. 5 (a) and (c) suggests that the working gas/medium mainly flows predominantly from left-to right-hand-side at φ_2 , and from right-to left-hand-side at φ_4 in Fig. 5 (b) and (d). Meanwhile, both D1 and D4 exhibit areas of reverse flow and acoustic streaming, such as near the right end of the stack at φ_2 and near the left end of the stack at φ_4 . These similarities suggest that the inlet diameter does not affect the flow direction and nonlinear phenomenon inside the flow fields of TAE models [56–58]. However, the color representing the maximum velocity region of D4 in Fig. 5 (c) and (d) is darker than that of D1 in (a) and (b). This implies that D4 is associated with a larger amplitude of the velocity compared to D1, indicating that the energy conversion process is more concentrated in D4 than in D1. Therefore, it can be concluded that the inlet diameter of the forced velocity does not affect the flow pattern of the internal flow field, but only affects the magnitude of the instantaneous velocity.

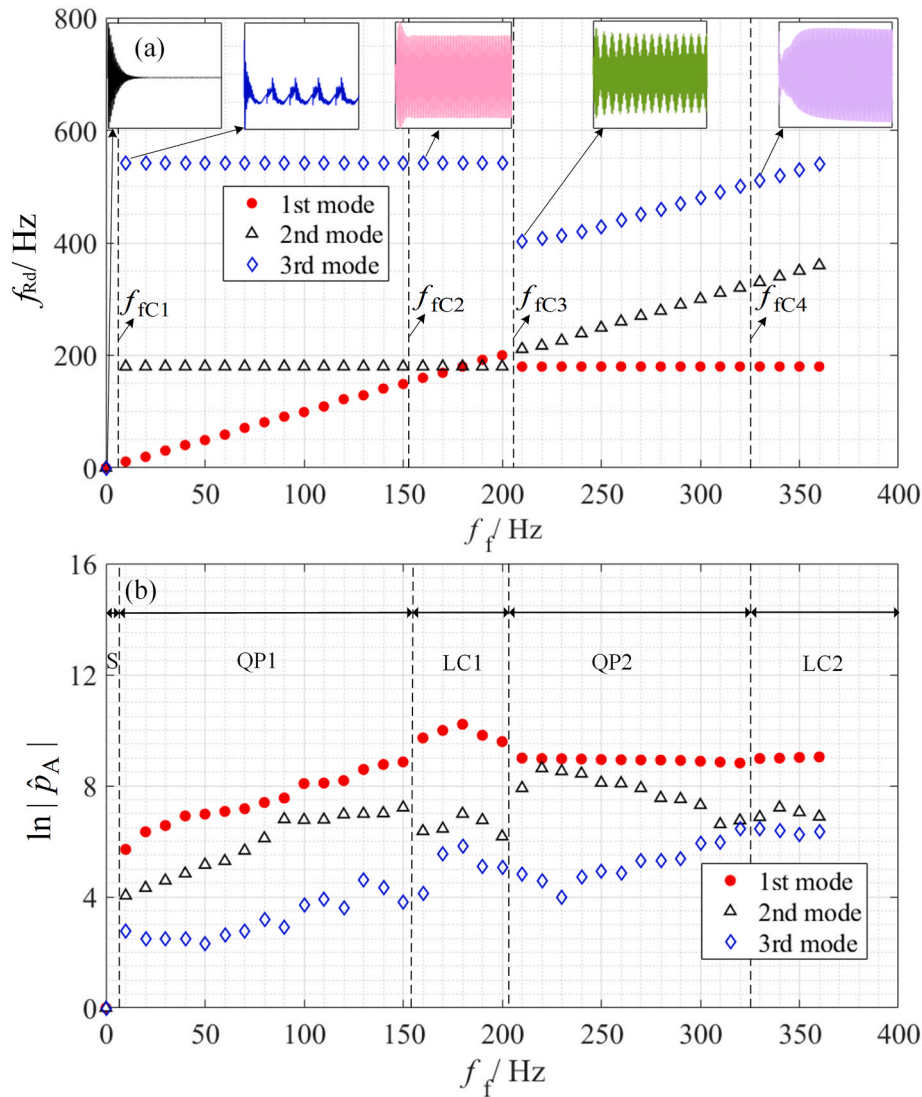


Fig. 9. The dominant (1st) and two harmonics (2nd and 3rd) of the decomposed acoustic oscillations (a) frequency and (b) natural logarithm-based pressure fluctuations of the SWTAE, induced by the forced velocity perturbations amplitude of 7.5 m/s and frequencies ranging from 0 to 360 Hz; time histories of acoustic pressure oscillations of the SWTAE at 0.1 Hz, 10 Hz, 160 Hz, 210 Hz and 330 Hz are presented in (a).

4. Thermodynamic characteristics and nonlinear effects of forced periodic velocity on TAE performances

4.1. Acoustic pressure output of TAE with different forced velocities

To examine the impacts of forced periodic velocity on the oscillation of the TAE, forced sinusoidal velocities with varying amplitudes v_{fA} (1 m/s, 2.5 m/s, 7.5 m/s, and 15 m/s) and frequencies f_f (0.1 Hz, 50 Hz, 90 Hz, 180 Hz, 230 Hz, 270 Hz, and 360 Hz) are applied to D4 model. The natural logarithm-based oscillation pressure amplitude ($\ln|\hat{p}'_A|$) and the dominant resonance frequency (f_{Rd}) of the TAE under different forcing velocities are presented in Fig. 6. The relevant values of the unforced model D0 are also displayed as the reference line.

The results presented in Fig. 6(a) show that the trends in the variations of $\ln|\hat{p}'_A|$ with respect to f_f are similar for different v_{fA} , and a larger v_{fA} has a greater impact on the $\ln|\hat{p}'_A|$ value. Note that $|\hat{p}'_A|$ is 0 under four forcing perturbations' amplitudes at $f_f = 0.1$ Hz $|\hat{p}'_A|$ is initially increased, maximized when f_f matches the SWTAE self-excited oscillation frequency ($f_s = 180$ Hz). Specifically, when v_{fA} is 15 m/s at 180 Hz, $|\hat{p}'_A|$ is increased by 327.90% compared to the unforced system D0. This

can be attributed to that constructive interference refers to the phenomenon, where the amplitudes of two or more waves of similar frequencies reinforce each other, resulting in an overall increase in the pressure perturbations' amplitude [59]. However, when f_f is far from f_s , $|\hat{p}'_A|$ is decreased and lower than that of the D0, indicating the attenuation of the self-excited thermoacoustic oscillations. The results indicate that the forced amplitude determines the magnitude of $|\hat{p}'_A|$, while the forced frequency determines the trend of $|\hat{p}'_A|$ variation. Then, a more detailed discussion of the forced frequency is provided. The ratio between the acoustic energy of the forced periodic velocity (E_{af}) and that of the self-excited oscillation of the TAE (E_{as}) is defined as γ_E , i.e., $\gamma_E = E_{af}/E_{as}$. From Fig. 6(b), we find that:

- (1) When v_{fA} is below 2.5 m/s, γ_E is within 0.11, indicating low forcing acoustic energy. At low forcing acoustical energy ($v_{fA} = 1$ m/s and 2.5 m/s), the forcing of the dominant oscillation mode, f_{Rd} , exhibits 'frequency lock-in' to the self-excited frequency ($f_s = 180$ Hz) [60]. For v_{fA} of 2.5 m/s at 0.1 Hz, 90 Hz, 180 Hz, and 270 Hz, phase diagrams of acoustic pressure fluctuations of the TAE from 0.1 s to 0.6 s are shown in Fig. 7. At 0.1 Hz, oscillation decays with time, showing 'quiescence' in steady

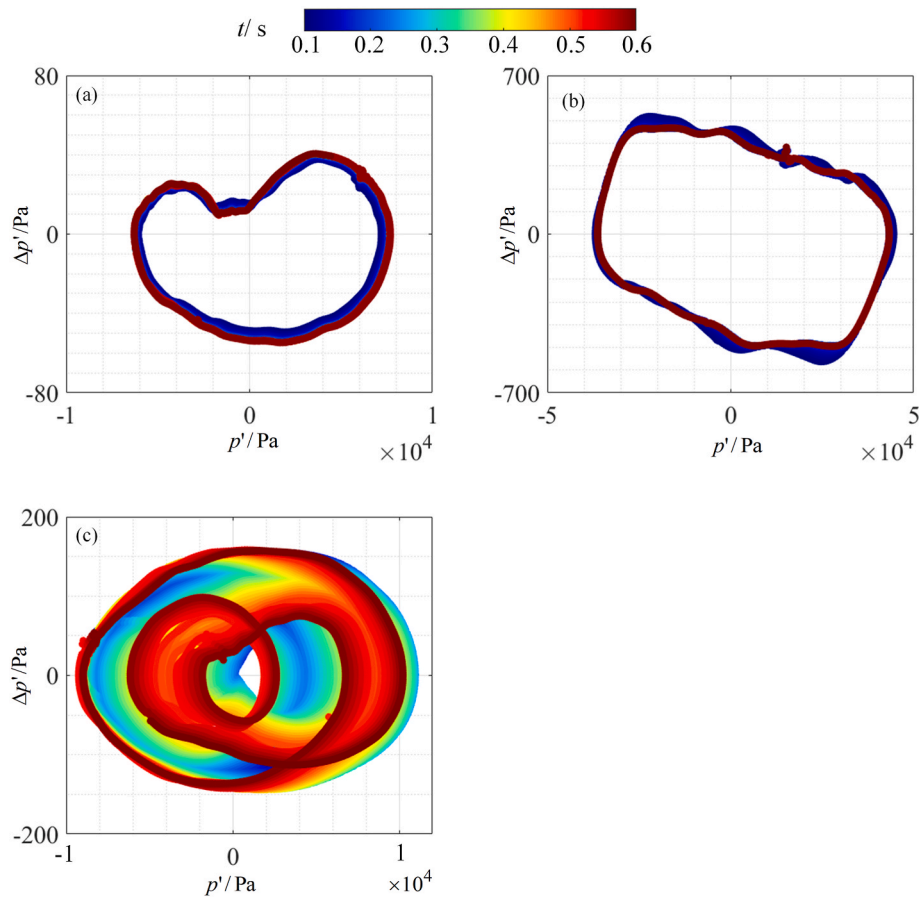


Fig. 10. Effect of the forcing periodic velocity perturbations on the phase diagrams illustrating the acoustic pressure fluctuations of the TAE over a span from 0.1 s to 0.6 s, with the forcing velocity perturbations' amplitude of 15 m/s at (a) 90 Hz (b) 180 Hz and (c) 270 Hz.

state. It is worth noting that two circles of the same color can be observed at 90 Hz (see Fig. 7(b)) and 270 Hz (see Fig. 7(d)). This indicates that the pressure gradient ($\Delta p'$) is not stable, and the system oscillates at two dominant frequencies at the same time [61]. This phenomenon is referred to as 'quasi-periodicity' [62]. On the contrary, at 180 Hz (see Fig. 7(c)), the limit cycle oscillation is occurred in the system.

- (2) At v_{iA} of 7.5 m/s, representing the medium-intensity forcing perturbations with γ_E of 0.33, numerical simulations are conducted for f_f from 0 to 550 Hz at 10 Hz intervals. Fig. 8 presents the natural logarithm-based pressure amplitude ($\ln|p'_A|$) and dominant frequency (f_{rd}) of the SWTAE under the medium-level forcing perturbations. At f_f between 160 and 200 Hz, $|p'_A|$ is increased significantly, reaching its peak at 180 Hz. When f_f is below 150 Hz or above 290 Hz, $|p'_A|$ is decreased and lower than that of DO. Therefore, it can be concluded that when f_f/f_s is between 0.89 and 1.11, forced sinusoidal velocity significantly increases thermoacoustic oscillation pressure. Conversely, a decreasing trend is observed when the value of f_f/f_s is less than 0.83 or greater than 1.61. Moreover, the dominant oscillation frequency is changed with the frequency of forcing periodic flow motions f_f before 220 Hz ($f_f/f_s \leq 1.22$), while frequency lock-in at the self-excited frequency after 220 Hz ($f_f/f_s > 1.22$). This phenomenon is known as 'bifurcation' and has been previously reported in Refs. [63,64].

To further study the phenomenon of Hopf bifurcation, $|p'_A|$ is decomposed into the dominant frequency (1st) and two higher har-

monics (2nd and 3rd) by FFT algorithm. The resulting frequencies and pressure components against different f_f are presented in Fig. 9. The plot reveals a transition in nonlinear system behaviors, with distinct oscillation areas: S (steady), QP1 (quasi-periodic-1), LC1 (limit cycle oscillation-1), QP2 (quasi-periodic mode), and LC2 (limit cycle oscillation-2) forms. At $f_f = 0.1$ Hz (S area), the pressure oscillations are gradually decaying, indicating the absence of self-excited oscillations. At $f_f = 10$ Hz (QP1 area), self-excited pressure oscillation starts, with a subcritical Hopf bifurcation from a stable fixed point to unstable quasi-periodic oscillation [65]. $|p'_A|$ increases with f_f in this area. 1st and 2nd modes of the pressure components exhibit similar magnitudes, indicating significant nonlinear phenomena in the oscillations waveforms. At $f_f = 160$ Hz (LC1 area), a supercritical Neimark-Sacker bifurcation leads to stable constant-amplitude oscillations [66]. The acoustic pressure primarily fluctuates at the first mode, resulting in the occurrence of limit cycle oscillation in the system. At $f_f = 210$ Hz (QP2 area), a subcritical Hopf bifurcation causes a quasi-periodicity 'beating' pattern in the time history, resulting from the co-existence of self-excited oscillation and forcing velocity perturbations. As f_f approaches the second-mode natural resonant frequency of the system, at $f_f = 330$ Hz, the steady-state response undergoes a supercritical Hopf bifurcation to limit-cycle oscillations. Therefore, the critical bifurcation frequencies are identified as 10 Hz (f_{fc1}), 160 Hz (f_{fc2}), 210 Hz (f_{fc3}), and 330 Hz (f_{fc4}). The theoretical mechanisms underlying these transitions and bifurcations are explained using periodic orbit theory, extensively by Venkatesan et al. [67]. The description of the theory is beyond the scope of this article, and therefore, it is not discussed here.

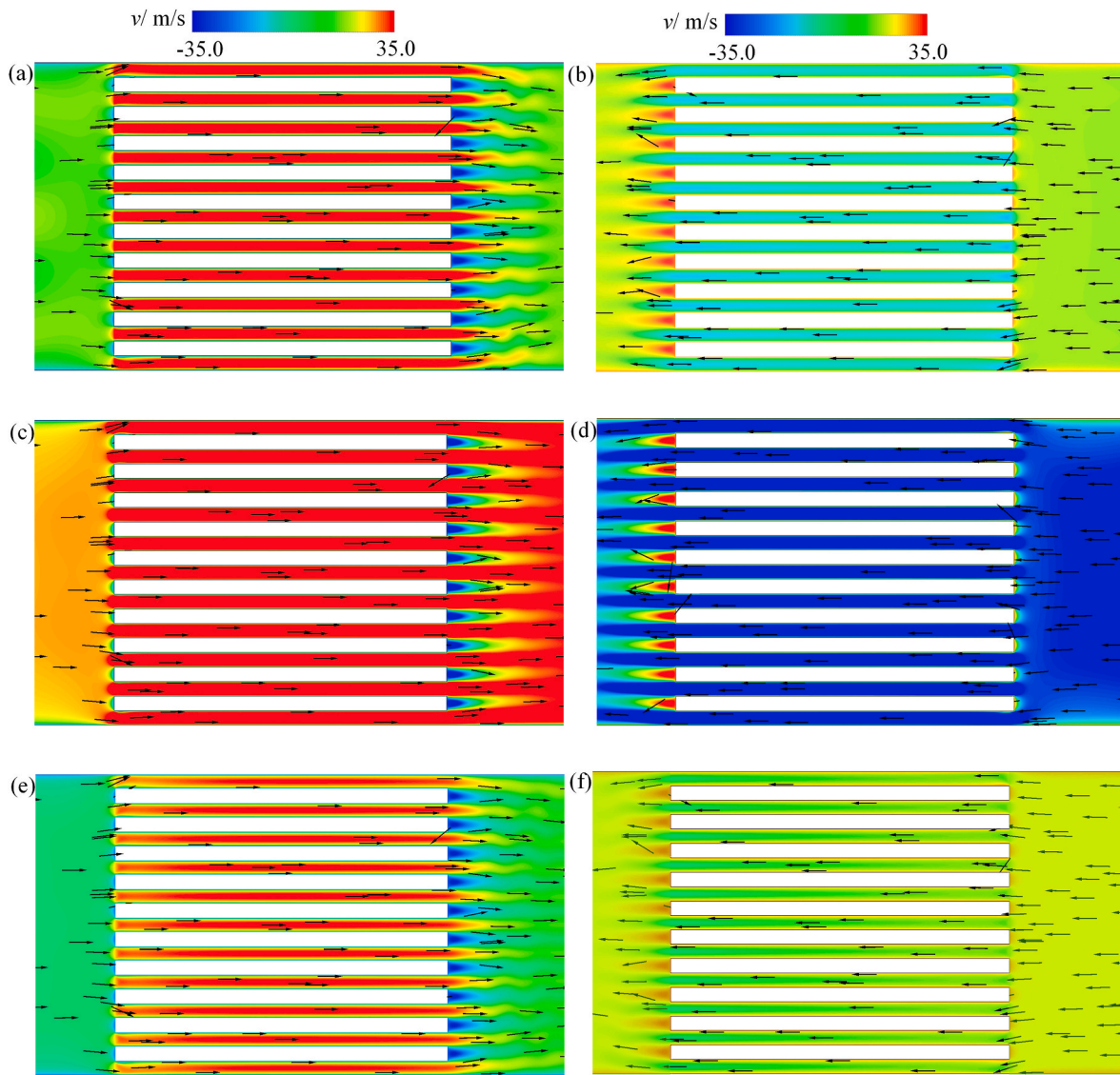


Fig. 11. Effect of forced periodic velocity on the flow velocity contours around the stack area of the TAE at velocity anti-nodes, (a) v_{hy1} at φ_2 , (b) v_{hy1} at φ_4 , (c) v_{hy2} at φ_2 , (d) v_{hy2} at φ_4 , (e) v_{hy3} at φ_2 , and (f) v_{hy3} at φ_4 .

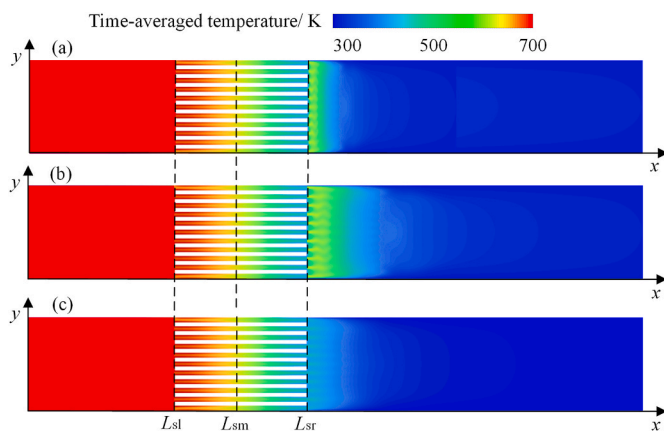


Fig. 12. Time-averaged mean temperature distribution of the working gas in the TAE, induced by forced velocities (a) v_{hy1} (b) v_{hy2} , and (c) v_{hy3} , respectively.

(3) When v_{fA} exceeds 15 m/s, corresponding to γ_E greater than 0.66, it is referred to as a larger forcing acoustic energy. When v_{fA} is 15 m/s, it can be seen from Fig. 6(b) that the resonance dominant frequency of the TAE responds to the forced frequency (f_f), except $f_f = 360$ Hz, where the TAE responds at the self-excited frequency ($f_s = 180$ Hz). Fig. 10 shows the phase diagram of acoustic pressure fluctuations with the forced velocity of 15 m/s at 90 Hz, 180 Hz, and 270 Hz from 0.1 s to 0.6 s, respectively. $\Delta p'$ and p' exhibit a significant increase at $f_f = 180$ Hz (see Fig. 10 (b)) compared to 90 Hz (see Fig. 10 (a)) and 270 Hz (see Fig. 10 (c)). This indicates the presence of intense thermoacoustic oscillations when f_f is 180 Hz. Moreover, Fig. 10(c) shows a 'swirl-shape' phase diagram, indicating the presence of multiple resonance frequencies and thus the nonlinearity of the system.

4.2. Thermodynamic characteristics of the TAE with different forced velocities

To investigate the effects of various forced amplitudes and frequencies on the inside flow fields of TAE, the instantaneous velocity in the vicinity of the stack area is analyzed. The forced velocities of the

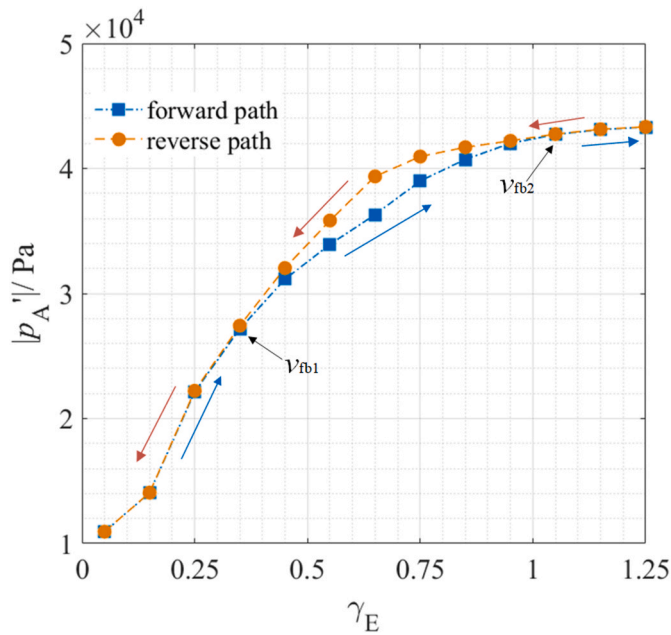


Fig. 13. Bifurcations in oscillation pressure amplitude of the TAE induced by variations in forced acoustic energy at a forcing frequency of 160 Hz through forward and reverse paths, illustrating the two-valued bifurcation zone and critical bifurcation values.

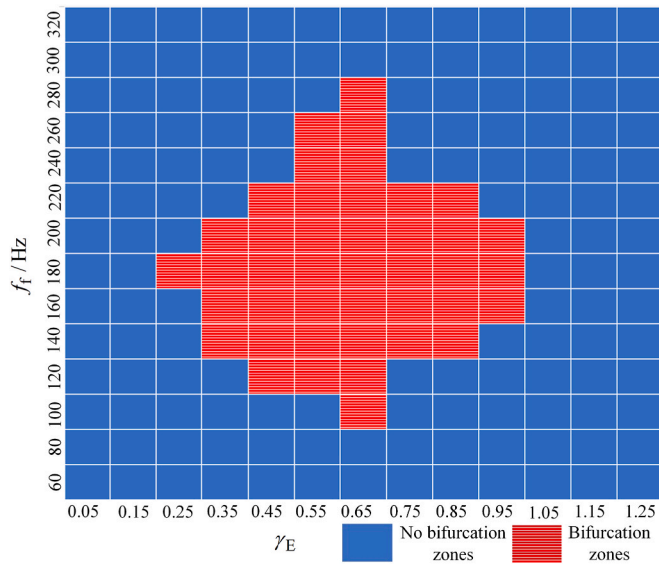


Fig. 14. The bifurcation zone of the acoustic oscillation pressure of the TAE, influenced by varying forced acoustic energy through forward and reverse paths, at forced frequencies ranging from 60 Hz to 320 Hz.

tested configuration are expressed as:

$$v_{hy1} = 1 \bullet \sin(2\pi \bullet 180 \bullet t) \quad (6a)$$

$$v_{hy2} = 7.5 \bullet \sin(2\pi \bullet 180 \bullet t) \quad (6b)$$

$$v_{hy3} = 7.5 \bullet \sin(2\pi \bullet 270 \bullet t) \quad (6c)$$

The instantaneous velocity around the stack area at velocity anti-node phases (φ_2 and φ_4) for TAE under v_{hy1} , v_{hy2} and v_{hy3} are illustrated in Fig. 11. The direction of the velocity vectors in Fig. 11 (a), (c) and (e) suggests that the working gas/medium flows predominantly from left-to right-hand-side at φ_2 , and from right-to left-hand-side at φ_4

in Fig. 11 (b), (d) and (f). Additionally, the flow fields of the TAE with v_{hy1} , v_{hy2} and v_{hy3} exhibit reverse flow and acoustic streaming at the same locations, i.e., near the right end of the stack at φ_2 and near the left end of the stack at φ_4 . Within the area of limit cycle oscillation, the internal flow fields of TAE under v_{hy1} , v_{hy2} and v_{hy3} present similarity, and their dominant frequency is equal to the self-excited frequency (f_s) of TAE. However, the color representing the maximum velocity region of the SWTAE with v_{hy2} is the darkest among the three forced systems, indicating the largest amplitude of the velocity vector. This is followed by the SWTAE with v_{hy1} . Conversely, the instantaneous velocity perturbation magnitude associated with v_{hy3} is observed to be smaller than that of v_{hy1} and v_{hy2} . Therefore, it can be inferred that a larger forcing velocity perturbations' amplitude at 180 Hz leads to a greater increase in velocity magnitude compared to a smaller forcing velocity amplitude at 270 Hz.

The temperature difference between the working gas/medium and the wall of the stack leads to the existence of non-zero heat fluxes at the wall surfaces, which in turn generates acoustic intensity in the SWTAE system. Fig. 12 shows the time-averaged mean temperature of the TAE system under v_{hy1} , v_{hy2} and v_{hy3} , respectively. Due to the thermoacoustic effect, with the middle position of the stack (L_{sm}) serving as the critical point, the mean temperature of the working gas in the left part of the stack and around the right end of the hot buffer is lower than the wall temperature of the stack (T_s), while the mean temperature of the working gas in the right part of the stack and around the left end of the resonator is higher than T_s . Moreover, the area affected by the time-averaged mean temperature of the working fluid is the largest around the stack area with v_{hy2} (see Fig. 12(b)). This difference indicates that among the three forced velocities, the motion of gas molecules is most pronounced under the influence of v_{hy2} .

4.3. Bifurcations of the TAE system by different paths of forced acoustic energy

To investigate the effect of continuously changing the forced acoustic energy ratio (γ_E) on the TAE system, Fig. 13 shows the resulting $|p'_A|$ under continuously changing γ_E at $f_f = 160$ Hz ($f_f/f_s = 0.89$). γ_E is systematically varied through both forward (by increasing γ_E from 0.05 to 1.25) and reverse paths (by decreasing γ_E from 1.25 to 0.05). It can be seen that $|p'_A|$ during the forward and reverse paths are the same when γ_E is either over γ_{E2} ($\gamma_{E2} = 1.05$) or below γ_{E1} ($\gamma_{E1} = 0.35$) at $f_f = 160$ Hz. When γ_E is between γ_{E1} and γ_{E2} , the curves for the forward and reverse paths form a two-valued bifurcation zone that is referred to as a 'hysteresis loop' [68,69]. γ_{E1} and γ_{E2} represent critical bifurcation values, indicating that when γ_E is within this range, $|p'_A|$ is larger on the reverse path compared to the forward path. Simulations are conducted at f_f ranging from 60 Hz to 320 Hz, and the bifurcation zones of $|p'_A|$ of the TAE concerning different γ_E and f_f are illustrated in Fig. 14. Bifurcation zones occur within the range of forced frequencies (f_f) from 100 Hz to 280 Hz ($0.56 < f_f/f_s < 1.56$). The bifurcation zones become more pronounced as f_f approaches 180 Hz from both sides, and the distribution of the bifurcation zones is the widest ($0.25 < \gamma_E < 0.95$) when f_f is at 180 Hz ($f_f/f_s = 1$).

4.4. Acoustic characteristics of the TAE system after terminating forced velocities

This section investigates the changes in the acoustic characteristics of forced TAE systems that have reached the steady state after terminating externally forced energy. Five forced velocities located in different oscillation areas are expressed as:

$$v_{IS} = 2.5 \bullet \sin(2\pi \bullet 0.1 \bullet t) \quad (7a)$$

$$v_{IQP1} = 1 \bullet \sin(2\pi \bullet 10 \bullet t) \quad (7b)$$

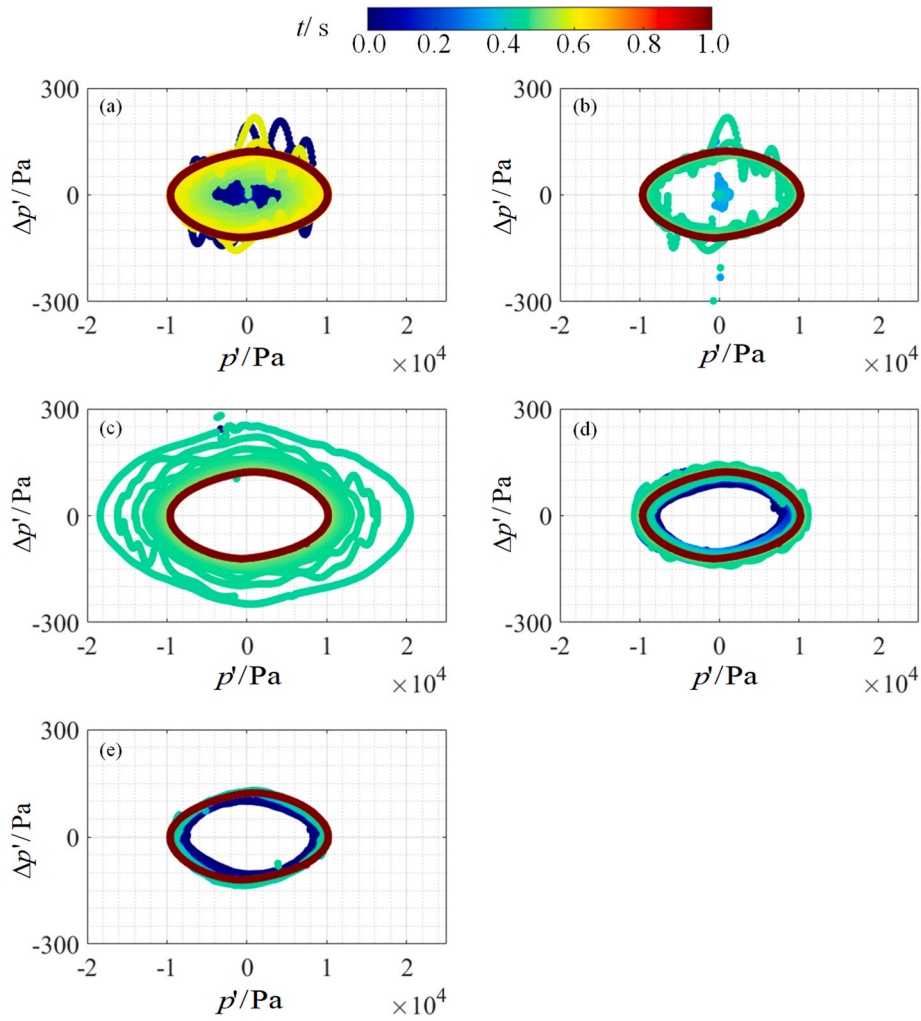


Fig. 15. Effect of forced periodic velocity on phase diagrams illustrating the acoustic pressure fluctuations of the TAE for 0.5 s before and after termination of forced velocity, with forced velocities (a) v_{IS} (b) v_{IQP1} , (c) v_{ILC1} (d) v_{IQP2} and (e) v_{ILC2} .

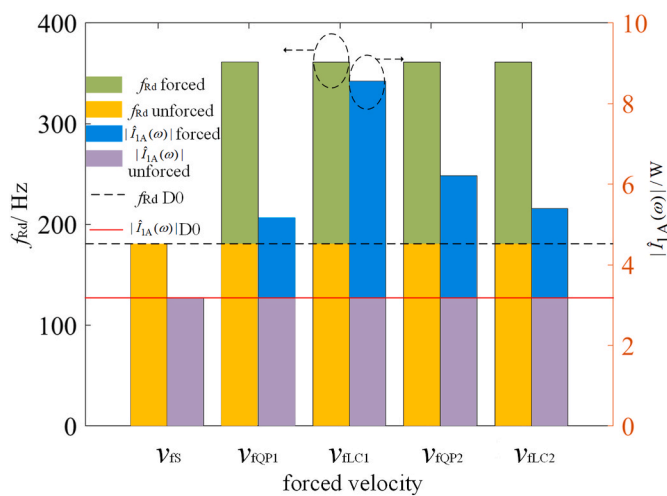


Fig. 16. Variation of absolute values of the fundamental-mode acoustic power amplitude and dominant frequency of forced TAE systems for 0.5 s before and after the termination of different forced velocities; D0 lines correspond to the relevant values of the unforced TAE model.

$$v_{ILC1} = 2.5 \cdot \sin(2\pi \cdot 180 \cdot t) \quad (7c)$$

$$v_{IQP2} = 7.5 \cdot \sin(2\pi \cdot 270 \cdot t) \quad (7d)$$

$$v_{ILC2} = 15 \cdot \sin(2\pi \cdot 360 \cdot t) \quad (7e)$$

After applying forced velocities for 0.5 s, the inputs are terminated. The phase diagrams of acoustic pressure fluctuations under v_{IS} , v_{IQP1} , v_{ILC1} , v_{IQP2} and v_{ILC2} with 0.5 s before and after the termination of the forced velocities are presented in Fig. 15. As shown in Fig. 15, the phase diagram at 1.0 s presents the same limit cycle oscillation regardless of the phase exhibited by the system under the forced velocity. This indicates that once the forced velocity is removed, the oscillation quickly transitions to self-excited oscillation. The absolute values of the fundamental-mode acoustic power amplitude and dominant frequency of the TAE under forced velocities v_{IS} , v_{IQP1} , v_{ILC1} , v_{IQP2} and v_{ILC2} for 0.5 s before and after the termination of the forced velocities are presented in Fig. 16. It further demonstrates that once the input velocity is unforced, the dominant frequency and acoustic power of the system become equal to those of D0. This indicates the prompt return of the system to its unforced state following the termination of the forced perturbations.

4.5. Acoustic output power and thermal efficiency of the TAE with different forced velocities

To investigate the TAE's energy conversion capacity under different

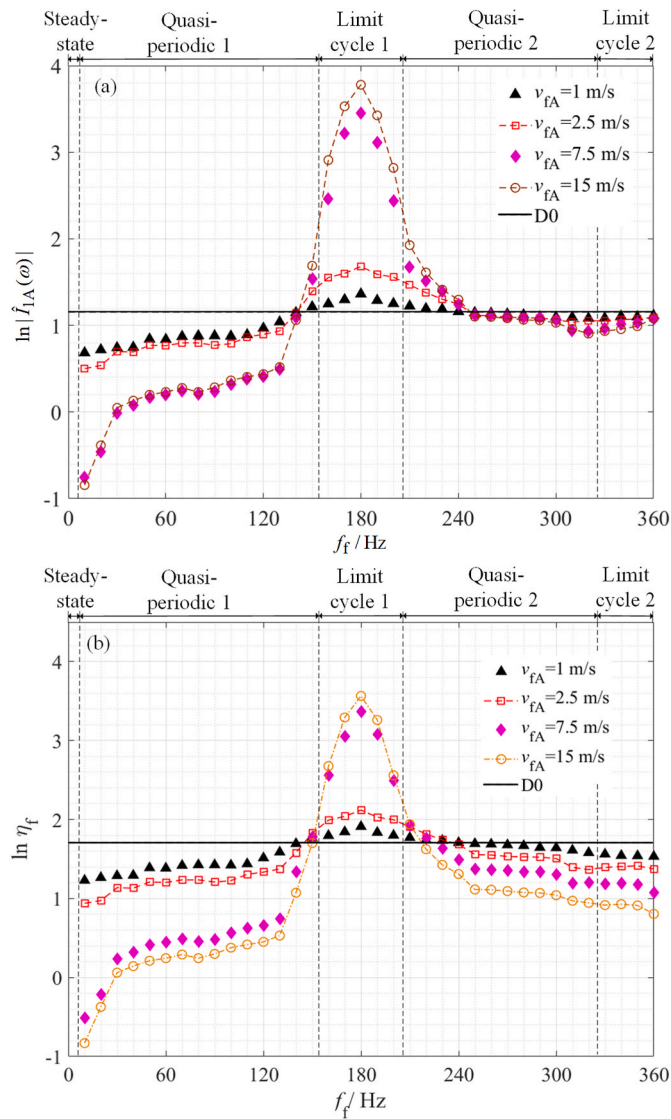


Fig. 17. Comparison of (a) natural logarithm-based fundamental-mode acoustic power amplitude and (b) thermal-acoustic efficiency obtained by the TAE with varying forced velocity amplitudes (1 m/s, 2.5 m/s, 7.5 m/s, and 15 m/s) with forced frequency ranging from 0 to 360 Hz, at intervals of 10 Hz; the D0 line corresponds to the relevant values of the unforced TAE model.

forced velocities, acoustic power corresponding to each forced velocity is obtained for various v_{fA} (1 m/s, 2.5 m/s, 7.5 m/s, and 15 m/s) and f_f (0–360 Hz). The resulting $\ln|\hat{I}_{1A}(\omega)|$ is depicted in Fig. 17(a). Moreover, the thermal-acoustic efficiency of the forced TAE system can be calculated by

$$\eta_f = \frac{|I(\omega)|}{\dot{Q}_{in} + \dot{E}_{af}} \approx \frac{|\hat{I}_{1A}(\omega)|}{\iint_{L_{st}} \dot{q}_t dx dy + \dot{E}_{af}} \quad (8a)$$

$$\dot{q}_t = -\kappa \frac{\partial T}{\partial x} \quad (8b)$$

where \dot{Q}_{in} and \dot{q}_t are the input heat power and the transversal heat fluxes at the stack walls, respectively. \dot{E}_{af} is forcing power of the periodic velocity. The time-averaged mean temperature of the working gas (T) under different forced velocities is obtained in Fig. 12, and the wall temperature of the stack (T_s) is set to decrease from 700 K at the left end of the stack (L_{sl}) to 300 K at the right end of the stack (L_{sr}) [70]. The temperature difference between T and T_s facilitates heat exchange

between the working gas and the stack, which is responsible for thermo-acoustic conversion [71–73]. Compared to the fundamental-order acoustic power $|\hat{I}_{1A}(\omega)|$, the contribution of the higher-order components ($|\hat{I}_{nA}(\omega)|$) is negligible, thus $|\hat{I}_{1A}(\omega)|$ is used instead of the value of the acoustic power ($|I(\omega)|$) in Eq. (8a). The natural logarithm-based thermal efficiency ($\ln \eta_f$) of the TAE is evaluated for various v_{fA} (1 m/s, 2.5 m/s, 7.5 m/s, and 15 m/s) and f_f (0–360 Hz), as shown in Fig. 17(b).

It can be observed from Fig. 17(a) that the general trend of $\ln|\hat{I}_{1A}(\omega)|$ variation with f_f remains roughly consistent for different v_{fA} . In the Steady-state area, the oscillation of the system attenuates, and the acoustic power dissipates. As the system oscillates in Quasi-periodic 1 and Quasi-periodic 2 areas, acoustic power increases as the f_f approaches f_s . Notably, when f_f is in the Limit cycle 1 area, $|\hat{I}_{1A}(\omega)|$ is significantly higher. Specifically, at $v_{fA} = 15$ m/s and $f_f = 180$ Hz, $|\hat{I}_{1A}(\omega)|$ is 863.95% and 747.11% greater than the D0 value and at $v_{fA} = 1$ m/s, respectively. Moreover, Fig. 17(b) indicates that η_f is also significantly increased when f_f is between 160 Hz and 200 Hz, i.e., $0.89 < f_f/f_s < 1.11$. η_f is observed to be influenced by f_f , with the effect of larger v_{fA} becoming more prominent. The maximum thermal efficiency value (35.34%) is obtained at a forced velocity of 15 m/s at 180 Hz, while the corresponding value for the unforced system D0 is 5.51%. Therefore, providing the TAE system with a forced frequency close to its self-excited frequency ($0.89 < f_f/f_s < 1.11$) can effectively enhance its acoustic power and thermal efficiency. Especially at $f_f/f_s = 1$, the maximum acoustic power and thermal efficiency are achieved (180 Hz in this model). The enhancement of TAE output performance and thermal efficiency becomes more prominent with larger forced velocity amplitudes.

5. Conclusions

In this work, numerical investigations using Computational Fluid Dynamics (CFD) are conducted on the full-scale standing-wave thermoacoustic engines (TAE) in presence of externally forcing flow perturbations. The primary focus is to explore the impacts of the forcing perturbations, including 1) the forcing perturbation frequencies, 2) its amplitudes, and 3) the inlet diameter of the externally forcing oscillations, on the thermo-acoustic energy conversion performance and nonlinear dynamics of thermoacoustic oscillations in these SWTAE systems. The key findings are listed as follows:

- Attenuation/Damping effect. Applying externally forcing pressure or velocity perturbations at the inlets may suppress or even completely attenuate heat-driven limit cycle oscillations in the SWTAEs by breaking up the coupling between thermal and acoustics effects.
- Effects of the inlet diameter. The effects of externally forcing periodic oscillations on SWTAEs with different inlet diameters of 1 mm, 7 mm, 14 mm, and 21 mm reveal a notable increase in the heat-driven acoustic output performance with a larger inlet diameter, while the oscillation frequency of the dominant mode remains constant/unchanged.
- observed nonlinear dynamics phenomena. The energy measure γ_E , representing the ratio of externally forcing perturbations' energy to that of self-excited heat-driven oscillations in the SWTAE, demonstrates the resonance frequency lock-in within the range $0.11 \leq \gamma_E \leq 0.66$. When the forcing perturbations' frequency is approaching the SWTAE's self-excited frequency, the pressure oscillations' amplitudes exhibit a two-valued bifurcation zone formed by the forward and backward paths of the externally forcing acoustical energy, referred to as a 'hysteresis loop'. Further investigations into the forcing periodic velocity perturbations reveal Hopf supercritical bifurcations, resulting in the transition of the perturbations' mode from steady state to quasi-periodic oscillations and limit cycle oscillations.

- Enhancing energy conversion performance. Dramatic enhancements in pressure oscillations' amplitude, sound pressure level (SPL), acoustic power, and thermo-acoustics energy conversion efficiency are observed, when the forcing perturbations' frequency f_f is approaching and close to that of the self-excited acoustic oscillations f_s (i.e. $0.89 < f_f/f_s < 1.11$). Maximum performance is observed to occur, when $f_f = f_s$ (180 Hz). These improvements can be further enhanced by increasing the amplitude of such externally forcing of periodic velocity perturbations.

The present results reveal the thermo-acoustics conversion and nonlinear dynamics behaviors in the SWTAE systems in presence of externally forcing perturbations. Optimizing the heat-driven acoustic output of the SWTAE can be achieved with a large inlet diameter and a large-amplitude externally forcing velocity perturbation at a frequency close to the self-excited thermoacoustic oscillation frequency. It is worth noting that the current CFD simulations are conducted basing on the simplified SWTAE systems. The practical thermoacoustic systems involve with complex boundary conditions and a larger flow/heat losses. This means that the present findings provide qualitative insights rather than quantitative ones.

CRedit authorship contribution statement

Lixian Guo: Writing – review & editing. **Dan Zhao:** Writing – review & editing, Writing – original draft, Validation, Supervision, Software, Resources, Project administration, Methodology, Investigation, Funding acquisition, Formal analysis, Data curation, Conceptualization. **Li Cheng:** Writing – review & editing, Writing – review & editing. **Xu Dong:** Writing – review & editing, Writing – original draft. **Jingyuan Xu:** Validation, Writing – review & editing.

Declaration of competing interest

The authors declare that they have no known competing financial interests or personal relationships that could have appeared to influence the work reported in this paper.

Data availability

Data will be made available on request.

Acknowledgments

We would like to acknowledge the financial support (452DISDZ) from the University of Canterbury, New Zealand. The first author would like to thank the faculty of Engineering, University of Canterbury for providing Ph.D. scholarship. Xu Dong would like to acknowledge the financial support from the project funded by Science Center for Gas Turbine Project (P2022-C-II- 003-001).

Appendix A. Supplementary data

Supplementary data to this article can be found online at <https://doi.org/10.1016/j.energy.2024.130634>.

References

- Garrett SL. Reinventing the engine. *Nature* 1999;399(6734):303–5.
- Backhaus S, Swift G. A thermoacoustic Stirling heat engine. *Nature* 1999;399(6734):335–8.
- Yang R, Wang J, Wu Z, Huang B, Luo E. Performance analysis of thermoacoustic plasma MHD generation. *Energy* 2023;263:125647.
- Rayleigh JWSB. *The theory of sound*. Macmillan; 1896.
- Tsuda K, Ueda Y. Critical temperature of traveling-and standing-wave thermoacoustic engines using a wet regenerator. *Appl Energy* 2017;196:62–7.
- Swift GW. *Thermoacoustics*. Springer Handbook of Acoustics; 2014. p. 247–63.
- Guedra M, Penelet G, Lotton P. Experimental and theoretical study of the dynamics of self-sustained oscillations in a standing wave thermoacoustic engine. *J Appl Phys* 2014;115(2).
- Ahmed F, Yu G, Luo E. A triboelectric nanogenerator attached to a thermoacoustic heat engine for power generation. *Energy Convers Manag* 2023;276:116482.
- Jin T, Huang J, Feng Y, Yang R, Tang K, Radebaugh R. Thermoacoustic prime movers and refrigerators: thermally powered engines without moving components. *Energy* 2015;93:828–53.
- Hariharan N, Sivashanmugam P, Kasthuriangan S. Effect of resonator length and working fluid on the performance of twin thermoacoustic heat engine—Experimental and simulation studies. *Comput Fluid* 2013;75:51–5.
- Rogoziński K, Nowak I, Nowak G. Modeling the operation of a thermoacoustic engine. *Energy* 2017;138:249–56.
- Guo L, Zhao D, Becker S. Temperature difference and stack plate spacing effects on thermodynamic performances of standing-wave thermoacoustic engines driven by cryogenic liquids and waste heat. *J Therm Sci* 2022;31(5):1434–51.
- Hamood A, Ja'fari M, Jaworski AJ. Synthetic jet flow driven by a standing-wave thermoacoustic heat engine. *Therm Sci Eng Prog* 2023;39:101725.
- Wang K, Hu ZC. Experimental investigation of a novel standing-wave thermoacoustic engine based on PCHE and supercritical CO₂. *Energy* 2023;282:128334.
- Yu G, Dai W, Luo E. CFD simulation of a 300 Hz thermoacoustic standing wave engine. *Cryogenics* 2010;50(9):615–22.
- Yu G, Wang X, Dai W, Luo E. Study on energy conversion characteristics of a high frequency standing-wave thermoacoustic heat engine. *Appl Energy* 2013;111:1147–51.
- Zhang Y, Shi X, Li Y, Zhang Y, Liu Y. Characteristics of thermoacoustic conversion and coupling effect at different temperature gradients. *Energy* 2020;197:117228.
- Chen G, Tang L, Yu Z, Mace B. Mode transition in a standing-wave thermoacoustic engine: a numerical study. *J Sound Vib* 2021;504:116119.
- Huang J, Yang R, Yang Y, Zhou Q, Luo E. Generalized thermoacoustic heat engines with unconventional working substances: a review. *Appl Energy* 2023;347:121447.
- Xu J, Hu J, Sun Y, Wang H, Wu Z, Hu J, Hochgreb S, Luo E. A cascade-looped thermoacoustic driven cryocooler with different-diameter resonance tubes. Part II: experimental study and comparison. *Energy* 2020;207:118232.
- Guo L, Zhao D, Yu G, Dong X. Numerical investigations on energy conversion performances in twin standing-wave thermoacoustic engines with various geometric and operational conditions. *Therm Sci Eng Prog* 2023;45:102134.
- Liu L, Yang P, Liu Y. Comprehensive performance improvement of standing wave thermoacoustic engine with converging stack: thermodynamic analysis and optimization. *Appl Therm Eng* 2019;160:114096.
- Yu Z, Mao X, Jaworski AJ. Experimental study of heat transfer in oscillatory gas flow inside a parallel-plate channel with imposed axial temperature gradient. *Int J Heat Mass Tran* 2014;77:1023–32.
- Ali U, Al Masalmeh Y, Abedrabbo S, Islam M, Janajreh I. Numerical simulation and experimental validation of thermoacoustic engine. *American Society of Mechanical Engineers*; 2022. V001T010A007.
- Di Meglio A, Massarotti N. CFD modeling of thermoacoustic energy conversion: a review. *Energies* 2022;15(10):3806.
- Kuzuu K, Hasegawa S. Effect of non-linear flow behavior on heat transfer in a thermoacoustic engine core. *Int J Heat Mass Tran* 2017;108:1591–601.
- Luo J, Zhou Q, Jin T. Numerical simulation of nonlinear phenomena in a standing-wave thermoacoustic engine with gas-liquid coupling oscillation. *Appl Therm Eng* 2022;207:118131.
- Guo L, Zhao D, Xu J, Tokhi MO, Karimi HR. Predicting unsteady heat-fluid interaction features and nonlinear acoustic behaviors in standing-wave thermoacoustic engines using unsteady RANS, LES and hybrid URANS/LES methods. *Int Commun Heat Mass Tran* 2023;142:106617.
- Chen G, Tang L, Mace BR. Bistability and triggering in a thermoacoustic engine: a numerical study. *Int J Heat Mass Tran* 2020;157:119951.
- Chen G, Tang L, Yu Z. Underlying physics of limit-cycle, beating and quasi-periodic oscillations in thermoacoustic devices. *J Phys Appl Phys* 2020;53(21):215502.
- Zhao D, Reyhanoglu M. Feedback control of acoustic disturbance transient growth in triggering thermoacoustic instability. *J Sound Vib* 2014;333(16):3639–56.
- Zhao D, Guan Y. Characterizing modal exponential growth behaviors of self-excited transverse and longitudinal thermoacoustic instabilities. *Phys Fluids* 2022;34(2):024109.
- Yazaki T, Sugioka S, Mizutani F, Mamada H. Nonlinear dynamics of a forced thermoacoustic oscillation. *Phys Rev Lett* 1990;64(21):2515.
- Kryuchkov NP, Yakovlev EV, Gorbunov EA, Couédel L, Lipaev AM, Yurchenko SO. Thermoacoustic instability in two-dimensional fluid complex plasmas. *Phys Rev Lett* 2018;121(7):075003.
- Zhao D. Thermoacoustic combustion instability control: engineering applications and computer codes. Elsevier; 2023. <https://doi.org/10.1016/C2020-0-03374-8>.
- Chen G, Tang L, Mace BR. Theoretical and experimental investigation of the dynamic behaviour of a standing-wave thermoacoustic engine with various boundary conditions. *Int J Heat Mass Tran* 2018;123:367–81.
- Qiu L, Lai B, Li Y, Sun D. Numerical simulation of the onset characteristics in a standing wave thermoacoustic engine based on thermodynamic analysis. *Int J Heat Mass Tran* 2012;55(7–8):2200–3.
- Zink F, Vipperman J, Schaefer L. CFD simulation of a thermoacoustic engine with coiled resonator. *Int Commun Heat Mass Tran* 2010;37(3):226–9.
- Bouramdane Z, Bah A, Alaoui M, Martaj N. Design optimization and CFD analysis of the dynamic behavior of a standing wave thermoacoustic engine with various geometry parameters and boundary conditions. *Int J Air-Conditioning and Refrigeration* 2023;31(1):1.

- [40] Alimohammadi S, Fanning E, Persoons T, Murray DB. Characterization of flow vectoring phenomenon in adjacent synthetic jets using CFD and PIV. *Comput Fluid* 2016;140:232–46.
- [41] Zink F, Viperman J, Schaefer L. CFD simulation of thermoacoustic cooling. *Int J Heat Mass Tran* 2010;53(19–20):3940–6.
- [42] Wu D, Xie X, Yang S. 2D simulation and experimental study of a horn influencing on an open-air traveling-wave thermoacoustic generator. *Energy Rep* 2022;8: 6845–55.
- [43] Chen G, Tang L, Mace B, Yu Z. Multi-physics coupling in thermoacoustic devices: a review. *Renew Sustain Energy Rev* 2021;146:111170.
- [44] Luo J, Zhou Q, Jin T. Theoretical and experimental investigation of acoustic field adjustment of a gas-liquid standing-wave thermoacoustic engine. *Energy* 2023; 276:127516.
- [45] Swift GW. Thermoacoustic engines. *J Acoust Soc Am* 1988;84(4):1145–80.
- [46] Chen G, Tang L, Mace BR. Modelling and analysis of a thermoacoustic-piezoelectric energy harvester. *Appl Therm Eng* 2019;150:532–44.
- [47] Zhang Z, Zhao D, Li S, Ji C, Li X, Li J. Transient energy growth of acoustic disturbances in triggering self-sustained thermoacoustic oscillations. *Energy* 2015; 82:370–81.
- [48] Xu J, Luo E, Hochgreb S. A thermoacoustic combined cooling, heating, and power (CCHP) system for waste heat and LNG cold energy recovery. *Energy* 2021;227: 120341.
- [49] He YL, Ke HB, Cui FQ, Tao WQ. Explanations on the onset and damping behaviors in a standing-wave thermoacoustic engine. *Appl Therm Eng* 2013;58(1–2): 298–304.
- [50] Murayama S, Gotoda H. Attenuation behavior of thermoacoustic combustion instability analyzed by a complex-network-and synchronization-based approach. *Phys Rev* 2019;99(5):052222.
- [51] Jin T, Yang R, Wang Y, Feng Y, Tang K. Low temperature difference thermoacoustic prime mover with asymmetric multi-stage loop configuration. *Sci Rep* 2017;7(1):7665.
- [52] El-Rahman A, Ahmed I, Abdel-Rahman E. Characteristic-based non-linear simulation of large-scale standing-wave thermoacoustic engine. *J Acoust Soc Am* 2014;136(2):649–58.
- [53] Ja'fari M, Jaworski AJ. On the nonlinear behaviour of oscillatory flow in a high pressure amplitude standing-wave thermoacoustic heat engine. *Int J Heat Mass Tran* 2023;201:123595.
- [54] Hariharan N, Sivashanmugam P, Kasthuriengan S. Influence of stack geometry and resonator length on the performance of thermoacoustic engine. *Appl Acoust* 2012;73(10):1052–8.
- [55] Zhu X, Walther JH, Zhao D, Haglind F. Transition to chaos in a cross-corrugated channel at low Reynolds numbers. *Phys Fluids* 2019;31(11):114107.
- [56] Allafi WA, Saat FAZM, Mao X. Fluid dynamics of oscillatory flow across parallel-plates in standing-wave thermoacoustic system with two different operation frequencies. *Engineering Science and Technology. Int J* 2021;24(1):41–9.
- [57] Zarch AB, Mazaheri K. A numerical investigation on stack sides thermo-gas dynamic in a large amplitude standing wave thermoacoustic engine. *Appl Therm Eng* 2023;234:121288.
- [58] Guan Y, Becker S, Zhao D, Xu J, Shahsavari M, Schluter J. Entropy generation and CO₂ emission in presence of pulsating oscillations in a bifurcating thermoacoustic combustor with a Helmholtz resonator at off-design conditions. *Aerospace Science and Technology* 2023;136:108204.
- [59] Sun Y, Zhao D, Ji C, Zhu T, Rao Z, Wang B. Large-eddy simulations of self-excited thermoacoustic instability in a premixed swirling combustor with an outlet nozzle. *Physics of Fluids* 2022;34(4):044112.
- [60] Tregidgo L, Wang Z, Gursul I. Frequency lock-in phenomenon for self-sustained roll oscillations of rectangular wings undergoing a forced periodic pitching motion. *Phys Fluids* 2012;24(11):117101.
- [61] Sun Y, Zhao D, Zhu X. Generation and Mitigation mechanism studies of nonlinear thermoacoustic instability in a modelled swirling combustor with a heat exchanger. *Aerospace* 2021;8(3):60.
- [62] Tang G, Gu X, Barber RW, Emerson D, Zhang Y. Lattice Boltzmann simulation of nonequilibrium effects in oscillatory gas flow. *Phys Rev* 2008;78(2):026706.
- [63] Kimura K, Takehiro S-I, Yamada M. Stability and bifurcation diagram of Boussinesq thermal convection in a moderately rotating spherical shell. *Phys Fluids* 2011;23 (7):074101.
- [64] Li X, Zhao D, Yang X. Experimental and theoretical bifurcation study of a nonlinear standing-wave thermoacoustic system. *Energy* 2017;135:553–62.
- [65] Kashinath K, Waugh IC, Juniper MP. Nonlinear self-excited thermoacoustic oscillations of a ducted premixed flame: bifurcations and routes to chaos. *J Fluid Mech* 2014;761:399–430.
- [66] Kashinath K, Li LK, Juniper MP. Forced synchronization of periodic and aperiodic thermoacoustic oscillations: lock-in, bifurcations and open-loop control. *J Fluid Mech* 2018;838:690–714.
- [67] Venkatesan A, Lakshmanan M. Bifurcation and chaos in the double-well Duffing–Van der Pol oscillator: numerical and analytical studies. *Phys Rev* 1997;56 (6):6321.
- [68] Juniper MP. Triggering in the horizontal Rijke tube: non-normality, transient growth and bypass transition. *J Fluid Mech* 2011;667:272–308.
- [69] Kabiraj L, Steinert R, Saurabh A, Paschereit CO. Coherence resonance in a thermoacoustic system. *Phys Rev* 2015;92(4):042909.
- [70] Zhao D, Ji C, Li S, Li J. Thermodynamic measurement and analysis of dual-temperature thermoacoustic oscillations for energy harvesting application. *Energy* 2014;65:517–26.
- [71] Agarwal H, Unni VR, Akhil K, Ravi N, Iqbal SM, Sujith R, Pesala B. Compact standing wave thermoacoustic generator for power conversion applications. *Appl Acoust* 2016;110:110–8.
- [72] Guan Y, Zhao D. Enhancing ammonia combustion with minimum hydrogen blended in presence of self-excited intermittent pulsating oscillations. *Physics of Fluids* 2023;35(5):054102.
- [73] Nader WB, Chamoun J, Dumand C. Optimization of the thermodynamic configurations of a thermoacoustic engine auxiliary power unit for range extended hybrid electric vehicles. *Energy* 2020;195:116952.